Energy & Environmental Science

ROYAL SOCIETY OF CHEMISTRY

PAPER

View Article Online
View Journal

Cite this: DOI: 10.1039/d3ee03896c

Electronic structure optimization of metal–phthalocyanine *via* confining atomic Ru for all-pH hydrogen evolution†

Zhenhui Kou,[ac] Yingnan Liu,[a] Wenjun Cui,[g] Bin Yang,[a] Zhongjian Li,[a] Raul D. Rodriguez,[e] Qinghua Zhang,[a] Chung-Li Dong,[f] Xiahan Sang,[g] Lecheng Lei,[a] Tao Zhang *[c] and Yang Hou *[abd]

Received 13th November 2023,
Accepted 9th January 2024

DOI: 10.1039/d3ee03896c

rsc.li/ees

The eco-friendly production of hydrogen under actual working conditions is a promising method to address the energy crisis. However, the lack of an effective proton source and the sluggish electrolyzed water process have resulted in a large kinetics difference in hydrogen evolution under different pH conditions. Herein, we report a robust strategy to break the kinetic barriers of hydrogen evolution for all-pH conditions through two-dimensional metal-polyphthalocyanine confined well-dispersed Ru atoms (Ru_{SA}@NiFe PPc). Benefiting from the synergistic effect between active Ru and conjugated polymers through interfacial Ru–N bonds, Ru_{SA}@NiFe PPc displays prominent reactivity for the HER under both acidic and alkaline conditions, achieving an ultrasmall overpotential of 12 mV at 10 mA cm^{-2} that is nearly 50 times smaller than that of pristine NiFe PPc and outperforming that of the benchmark Pt/C catalyst, and durable stability ~160 000 s at 200 mA cm^{-2}. We further demonstrate that a high-performance membrane electrode assembly device with Ru_{SA}@NiFe PPc and a commercial IrO_2 anode achieves a current density of 2.0 A cm^{-2} at a low voltage of only 2.27 V. Theoretical calculations reveal that the electronic structure optimization through Ru–N bridges induces the acceleration of activation/dissociation of water and adsorption of *H, thus breaking the deadlock of all-pH HER kinetics.

Broader context

Facing the gap of hydrogen evolution reaction kinetics under different conditions, recently, the introduction of noble-metal single atoms has been considered an effective way to boost electrocatalytic activity. However, electrochemical stability is poor under different conditions and the loaded metals are prone to precipitation and agglomeration on traditional substrates (such as metal oxides or hydroxides, *etc.*). Meanwhile, the complex composition of conventional supports hinders the exploration of the structure–activity relationship. Herein, we construct a high-activity all-pH electrocatalyst of two-dimensional metal-polyphthalocyanine (NiFe PPc) with clear and stable networks confining atomic Ru, through the electrochemical deposition method. Benefiting from the electronic coupling effect from Ru–N bridges on NiFe PPc, the Ru_{SA}@NiFe PPc shows remarkable all-pH HER activity, achieving a low overpotential of 12 mV to reach 10 mA cm^{-2} current density, which is nearly 50 times smaller than that of pristine NiFe PPc and outperforms that of the benchmark Pt/C catalyst. We further demonstrate that proton exchange membrane water electrolysis (PEMWE) with Ru_{SA}@NiFe PPc and a commercial IrO_2 anode achieves a current density of 2.0 A cm^{-2} at a low voltage of only 2.27 V. And more importantly, we further demonstrate an alkaline electrolyzer with Ru_{SA}@NiFe PPc and a stainless steel mesh (SSM) anode. The Ru_{SA}@NiFe PPc‖SSM system displays excellent performance, achieving current densities of 1.0 A cm^{-2} and 2.0 A cm^{-2} at cell voltages of 1.64 V and 1.72 V, respectively. Density functional theory calculations illustrate that the electronic structure of NiFe PPc is modulated by the construction of Ru–N bridges for optimizing the thermodynamics of adsorption of H* and adsorption/activation of H_2O, and finally boosting HER activity under different reaction conditions.

[a] *Key Laboratory of Biomass Chemical Engineering of Ministry of Education, College of Chemical and Biological Engineering, Zhejiang University, Hangzhou 310027, China. E-mail: yhou@zju.edu.cn*
[b] *Institute of Zhejiang University-Quzhou, 78 Jiuhua Boulevard North, Quzhou 324000, China*
[c] *Key Laboratory of Marine Materials and Related Technologies, Ningbo Institute of Materials Technology and Engineering, Chinese Academy of Sciences, Ningbo 315201, China. E-mail: tzhang@nimte.ac.cn*
[d] *Donghai Laboratory, Zhoushan, 316021, China*
[e] *Tomsk Polytechnic University, 30 Lenin Ave, Tomsk 634050, Russia*
[f] *Research Center for X-ray Science & Department of Physics, Tamkang University, New Taipei City, 25 137, Taiwan*
[g] *Research and Testing Centre of Material School of Materials Science and Engineering, Wuhan University of Technology, Wuhan, 430070, China*
† Electronic supplementary information (ESI) available. See DOI: https://doi.org/10.1039/d3ee03896c

The synthesis strategies of hydrogen have received wide attention because they play a key role in the essential chemicals' synthesis and energy conversion.[1–4] Electrocatalytic water splitting is regarded as an attractive method but also suffers from slow reaction kinetics.[5–12] Currently, it is well known that noble-metal (*e.g.*, Pt, Ru, Ir, *etc.*) based materials are the benchmark for water splitting.[13–15] However, their high price and poor stability strongly limit this technology, meanwhile, hydrogen evolution reaction (HER) kinetics is typically one to a few orders of magnitude lower in neutral or alkaline media than in acid,[16–20] and even on Pt-based catalysts.[16,17] It is therefore of technical significance to construct low-cost but fast-kinetics electrocatalysts, especially those that perform well under wide-range pH conditions.

Currently, conjugated microporous polymer (CMP) based materials with tunable electronic properties and a clear network structure are receiving growing interest in electrocatalysis.[21,22] Among them, highly π-conjugated metal phthalocyanine (MPc) with $M–N_4$ high activity sites shows great potential for boosting the all-pH HER, owing to highly tailorable molecular structures and chemically robust structures under harsh conditions.[23,24] However, pristine organic-based materials usually suffer from poor conductivity and rare active sites, when directly used to promote electrocatalytic processes.[25,26] Moreover, when participating in the HER process, the macrocycle networks could prevent short *H binding distances and thus follow the sluggish kinetic reaction pathway.[24] Recently, the anchoring of atomic noble metals has been proposed as an effective way to accelerate reaction kinetics.[27–30] Among them, Ru displayed attractive prospects, due to its strong water dissociation ability,[31] favorable bond strength with hydrogen, and competitive price compared with Pt.[7] However, the modulation of catalytic performance based on interfacial bond bridging formed by traditional metal oxide and hydroxide substrates is unsatisfactory for obtaining durability under harsh conditions.[32] Meanwhile, the complicated composition of traditional base-materials seriously prevents the exploration of the structure–activity relationship and reaction mechanism.[33,34] Therefore, developing novel catalyst carriers to optimize the activity is a critical but challenging task. In this regard, the reciprocal decoration between noble-metal species and MPc with clear and stable networks is expected to be an efficient catalyst for the all-pH HER.

In this work, we synthesized an electrocatalyst composed of two-dimensional MPc confined atomic Ru species (Ru_{SA}@NiFe PPc) for the all-pH HER by a facile electrochemical deposition strategy. Benefiting from the electronic coupling effect from Ru atoms and NiFe PPc, the as-synthesized catalyst optimized the reaction pathway. Specifically, the Ru_{SA}@NiFe PPc showed a remarkable HER activity, achieving a low overpotential of 12 mV to reach 10 mA cm^{-2} current density and a small Tafel slope of 31 mV dec^{-1}, which outperformed those of the benchmark Pt/C and most reported catalysts (*i.e.*, overpotential normally over 30–50 mV at 10 mA cm^{-2}; see details in Table S1, ESI†). Density functional theory (DFT) calculations suggested that the Ru_{SA}@NiFe PPc followed a favorable Volmer–Tafel pathway, in which the electronic structure of NiFe PPc can be modulated by the construction of Ru–N bridges, for optimizing the thermodynamics of adsorption of H* and adsorption/activation water, and contributing to the improvement of HER activity under different reaction conditions.

Before synthesizing Ru_{SA}@NiFe PPc, a two-dimensional NiFe PPc substrate was firstly fabricated according to the method reported in previous works.[35,36] The resultant Ru_{SA}@NiFe PPc with a clear Ru–N configuration was obtained *via* electrochemical deposition of Ru(IV) salts on a two-dimensional NiFe PPc network. Notably, the synthetic procedure was completed at room temperature and atmospheric pressure without harsh operations. As shown in Fig. 1a, electrochemical deposition of Ru species was conducted by performing cyclic voltammetry scans (Fig. S1, ESI†), using a three-electrode cell with NiFe PPc supported on carbon paper as the working electrode and the electrolyte consisting of 0.5 M H_2SO_4 with $(NH_4)RuCl_6$. The N-site-rich surface on the NiFe PPc is expected to interact with or adsorb the Ru cations, which promotes the incorporation of Ru atoms onto the conjugated polymer support. Coincidentally, during this process, we obviously observed that the original yellow electrolyte gradually turns into transparent (Fig. S2, ESI†), which is well consistent with the above assumption that the Ru cations moved near the working electrode and then were trapped. After multiple-scanning cycles, Ru atoms were immobilized on the NiFe PPc surface for producing Ru_{SA}@NiFe PPc. To illustrate the universality and robust characteristics of this synthesis method, Ru_{SA}@-bulk-phase NiFe PPc, Pt_{SA}@NiFe PPc as well as Pd_{SA}@NiFe PPc could also be synthesized by the same process, except for only replacing the metal salts in the electrolyte.

The results of electron microscopy showed that the morphology of bulk-phase NiFe PPc was not destroyed through the electrochemical deposition (Fig. S3, ESI†). Furthermore, the existence and uniform distribution of C, N, Ni, Fe, and Ru elements on the bulk-phase NiFe PPc and Ru_{SA}@NiFe PPc were observed (Fig. 1b and Fig. S4, ESI†), indicating the successful anchoring of Ru species by electrochemical deposition. Raman and UV-Vis spectra were utilized to prove the structural stability of the NiFe PPc before and after loading Ru. The results showed that the conjugated networks had been well preserved without structural damage (Fig. S5, ESI†). X-ray diffraction (XRD) patterns (Fig. S6, ESI†) confirmed the 2D nanostructure of Ru_{SA}@-NiFe PPc,[36,37] and no diffractions associated with Ru particles were observed on Ru_{SA}@NiFe PPc. And the high-resolution transmission electron microscopy (TEM) images also demonstrated the absence of Ru particles (Fig. S7, ESI†). Furthermore, the single Ru atoms present in the Ru_{SA}@NiFe PPc were directly verified by aberration-corrected high-angle annular dark-field scanning transmission electron microscopy (AC HAADF-STEM), as reflected by the highly dispersed bright dots associated with single Ru atoms on the NiFe PPc (Fig. S8, ESI†). The loading amount of Ru atoms was determined to be 0.7 wt% in Ru_{SA}@-NiFe PPc, based on inductively coupled plasma-optical emission spectroscopy (ICP-OES) analysis (Table S2, ESI†). The atomic force microscopy (AFM) image revealed the ultra-thin trait of Ru_{SA}@NiFe PPc, possessing a thickness of about ~3.7 nm (Fig. 1c). The TEM image further displayed that the Ru_{SA}@NiFe PPc consisted of only a few layers of NiFe PPc (Fig. 1d).

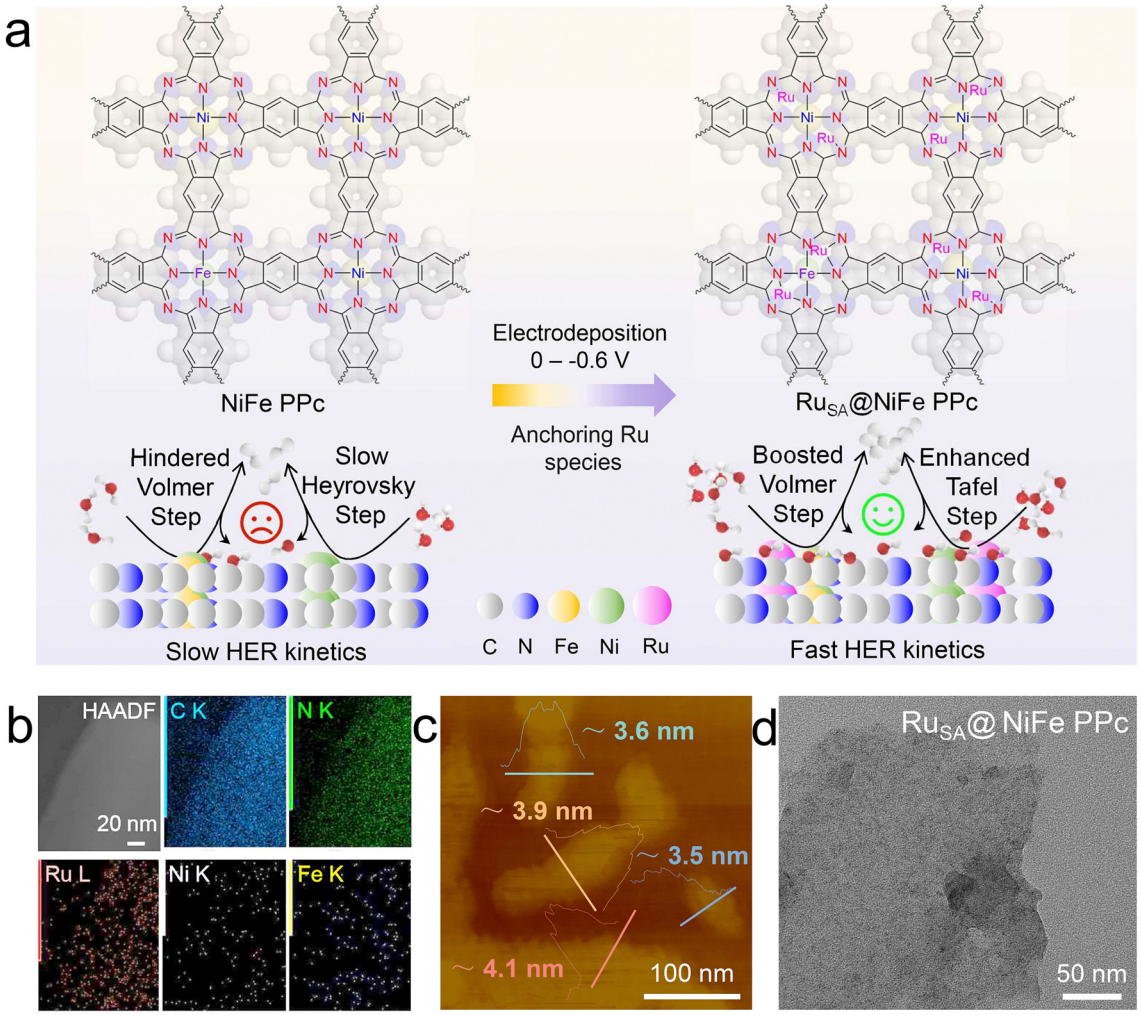

Fig. 1 Synthesis strategy, structural analysis and electron microscopy. (a) Schematic illustration of the synthetic strategy for the Ru$_{SA}$@NiFe PPc. (b) HAADF-STEM and corresponding EDX elemental mapping images of Ru$_{SA}$@NiFe PPc. (c) AFM image of Ru$_{SA}$@NiFe PPc. (d) TEM image of Ru$_{SA}$@NiFe PPc.

To unravel the chemical composition and electronic structure of Ru$_{SA}$@NiFe PPc, the X-ray photoelectron spectroscopy (XPS) test was conducted. The XPS survey spectrum of Ru$_{SA}$@NiFe PPc proved the successful introduction of Ru atoms (Fig. S9, ESI†). Through in-depth analysis of high-resolution Ni 2p XPS spectra (Fig. 2a), the positive shifts of 0.5 eV and 0.4 eV were observed after introduction of Ru atoms, which was ascribed to the stronger electronegativity of Ru atoms, resulting in the electronic coupling of Ru and NiFe PPc.[29,38,39] The high-resolution Ru 3p XPS spectra exhibited two spin–orbit splitting located at 463.86 eV and 486.04 eV, intermediate between Ru(0) and Ru(IV) (Fig. 2b). The high-resolution N 1s XPS spectra of Ru$_{SA}$@NiFe PPc were dominated by the metal–N bond and C–N bond located at 400.3 eV and 398.9 eV, respectively (Fig. S10, ESI†).[40] It is worth noting that the N 1s peaks were shifted to higher binding energy after Ru loading, indicating that the electron density of the N atoms became lower, which could be explained by considering that the electron structure would be changed through the formation of Ru–N bonds.[41] To support the above results, we firstly completed DFT calculations to prove the priority of Ru binding sites, through analyzing the difference of binding energy between the different sites on NiFe PPc, including Ni sites, Fe sites, N sites near Ni sites, and N sites near Fe sites (Fig. S11, ESI†). It could be clearly seen that the binding energies of Ru atoms to the N sites near Fe sites and Ni sites are 275.53 eV and 272.75 eV, respectively, which are close to or higher than the binding energies of Fe or Ni sites (275.72 eV and 271.59 eV). The results demonstrated that the Ru atoms would preferentially bond to N sites on the metal phthalocyanine networks.

We further performed X-ray absorption near-edge structure spectroscopy (XANES) and extended X-ray absorption fine structure (EXAFS) to investigate localized electronic states and coordination environments of Ru atoms in Ru$_{SA}$@NiFe PPc at the atomic level. Ru foil and RuO_2 were used as references. At first, Ru K-edge XANES spectra of Ru$_{SA}$@NiFe PPc (Fig. 2c) showed that the edge energy was higher than that of the Ru foil, which demonstrated that the Ru$_{SA}$@NiFe PPc exposed positively charged single-atomic $Ru^{\delta+}$ ($0 < \delta$).[42] The $Ru^{\delta+}$ single-atom would have the tendency to chemically coordinate with N or C or metal sites (Ni or Fe), *etc.* And then, through the Fourier-

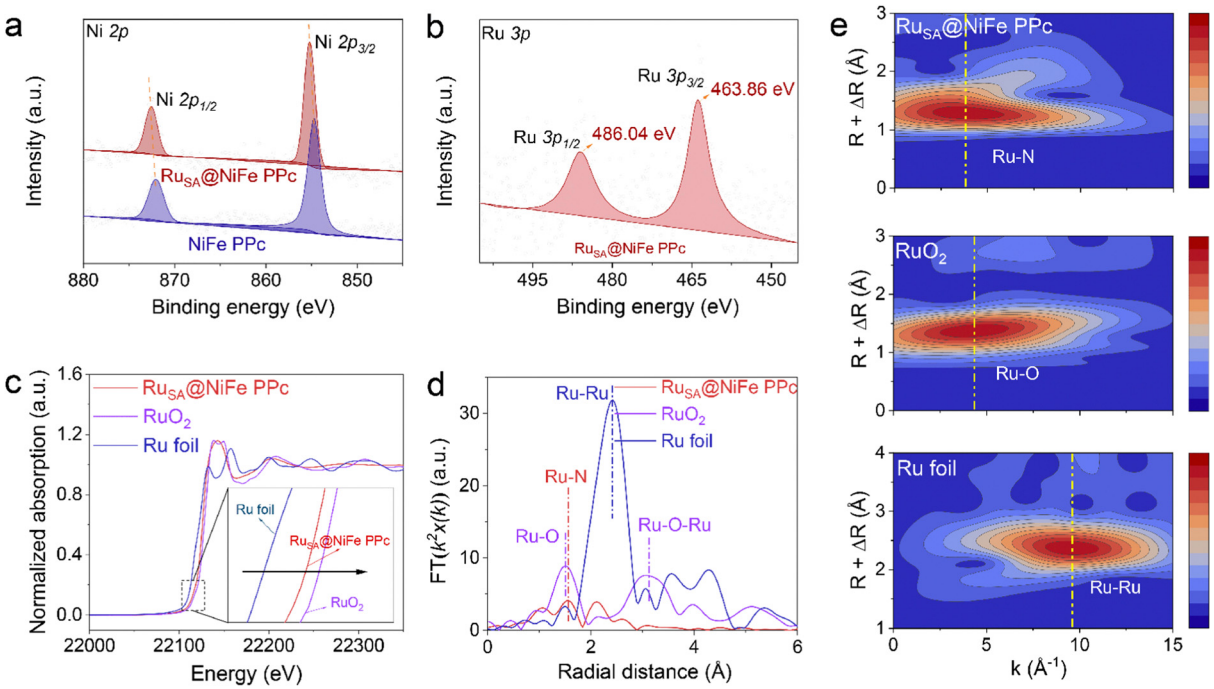

Fig. 2 Structural characterization by X-ray spectroscopy. (a) High-resolution Ni 2p XPS spectra of Ru_{SA}@NiFe PPc and NiFe PPc. (b) High-resolution Ru 3p XPS spectra of Ru_{SA}@NiFe PPc and NiFe PPc. (c) XANES spectra at the Ru K-edge of Ru_{SA}@NiFe PPc, RuO_2 and Ru foil. (d) Fourier-transform EXAFS spectra of c. (e) WT-EXAFS plots of Ru_{SA}@NiFe PPc, RuO_2, and Ru foil.

transform EXAFS (FT-EXAFS) spectra in Fig. 2d, a first shell Ru–N peak is observed at around 1.55 Å, between the Ru foil at 2.47 Å and RuO_2 at 1.48 Å in Ru_{SA}@NiFe PPc. Moreover, the contribution of Ru–Ru and Ru–O–Ru bonds at 3.10 Å for the Ru foil and RuO_2 was absent for Ru_{SA}@NiFe PPc, strongly illustrating that there are no Ru particles/clusters mainly corresponding to Ru–N bonds. To further precisely clarify the atomic dispersion and coordination conditions of Ru species, wavelet transform EXAFS (WT-EXAFS) was performed. In Fig. 2e, Ru_{SA}@NiFe PPc displayed a different intensity maximum with the Ru foil and RuO_2. Specifically, the intensity maximum of 3.6 $Å^{-1}$ for Ru_{SA}@NiFe PPc was lower than those of Ru foil (9.4 $Å^{-1}$) and RuO_2 (4.2 $Å^{-1}$), confirming the coordination environment of Ru atoms in Ru_{SA}@NiFe PPc. The fitting EXAFS results again proved the existence of coordinative Ru–N bonds (Fig. S12 and Table S3, ESI†), which was in accordance with the analysis of the above calculations results. Therefore, all the above results confirmed that Ru atoms have been successfully introduced into the NiFe PPc through the strong electronic coupling with the conjugated network substrate *via* N atoms.[29,40,43,44]

The HER performances of Ru_{SA}@NiFe PPc were evaluated in multiple electrolytes, including 0.5 M H_2SO_4, 1.0 M KOH, and 0.1 M phosphate buffer solution (PBS, pH = 3, pH = 7, and pH = 10), respectively. The catalyst NiFe PPc and commercial Pt/C were also tested as references. Compared with the counterparts, Ru_{SA}@NiFe PPc exhibited a significantly higher HER catalytic activity benefiting from the doped Ru species (Fig. 3a). A much lower overpotential of 40 mV in 0.5 M H_2SO_4 and 12 mV in 1.0 M KOH at a current density of 10 mA cm^{-2} over Ru_{SA}@NiFe PPc was obtained than that of commercial Pt/C and NiFe PPc (691 mV in 0.5 M H_2SO_4 and 604 mV in 1.0 M KOH) (Fig. 3a and Fig. S13, ESI†). The reliability of the test results was verified by calibration of the reference electrode of Ag/AgCl (Fig. S14, ESI†). More importantly, at a higher current density, Ru_{SA}@NiFe PPc still displayed a profitable average overpotential (Fig. 3b, c and Fig. S15, Table S4, ESI†). In order to further highlight the advantages of Ru_{SA}@NiFe PPc, we evaluated its HER activity with commercial Pt/C in many types of electrolysis environment including 0.1 M PBS (pH = 3, pH = 7, and pH = 10), in which the Ru_{SA}@NiFe PPc always outperformed the commercial Pt/C (Fig. S16, ESI†). Besides, the Ru_{SA}@NiFe PPc displayed a low Tafel slope of 31 mV dec^{-1} (Fig. 3d), manifesting a rapid HER kinetics originating from the superiority of introducing Ru atoms. The low electrochemical resistance of Ru_{SA}@NiFe PPc of ~4.0 Ω (Fig. S17, ESI†) further implied improvement of charge transfer and superior HER kinetics for Ru_{SA}@NiFe PPc. To support the fast kinetics of Ru_{SA}@NiFe PPc, an *in situ* EIS test was performed from open circuit potential (OCP) to an overpotential of 140 mV (Fig. S18a and b, ESI†). Through observing the trend and size changes of the Nyquist plot semicircle, the reaction kinetics and adsorption of reactants could be explored. It was clearly observed that the direct change of trend size in the Nyquist plot semicircle for Ru_{SA}@NiFe PPc was faster than that of the NiFe PPc, which implies superior kinetics and adsorption of the reactants after incorporating Ru atoms on NiFe PPc, attributed to the formed Ru–N coordination for accelerating HER kinetics. And these Nyquist plots were further fitted by an equivalent circuit to assess the parameter R_{ct} that represents the adsorption resistance of oxygen-containing reactive species. The results showed that the

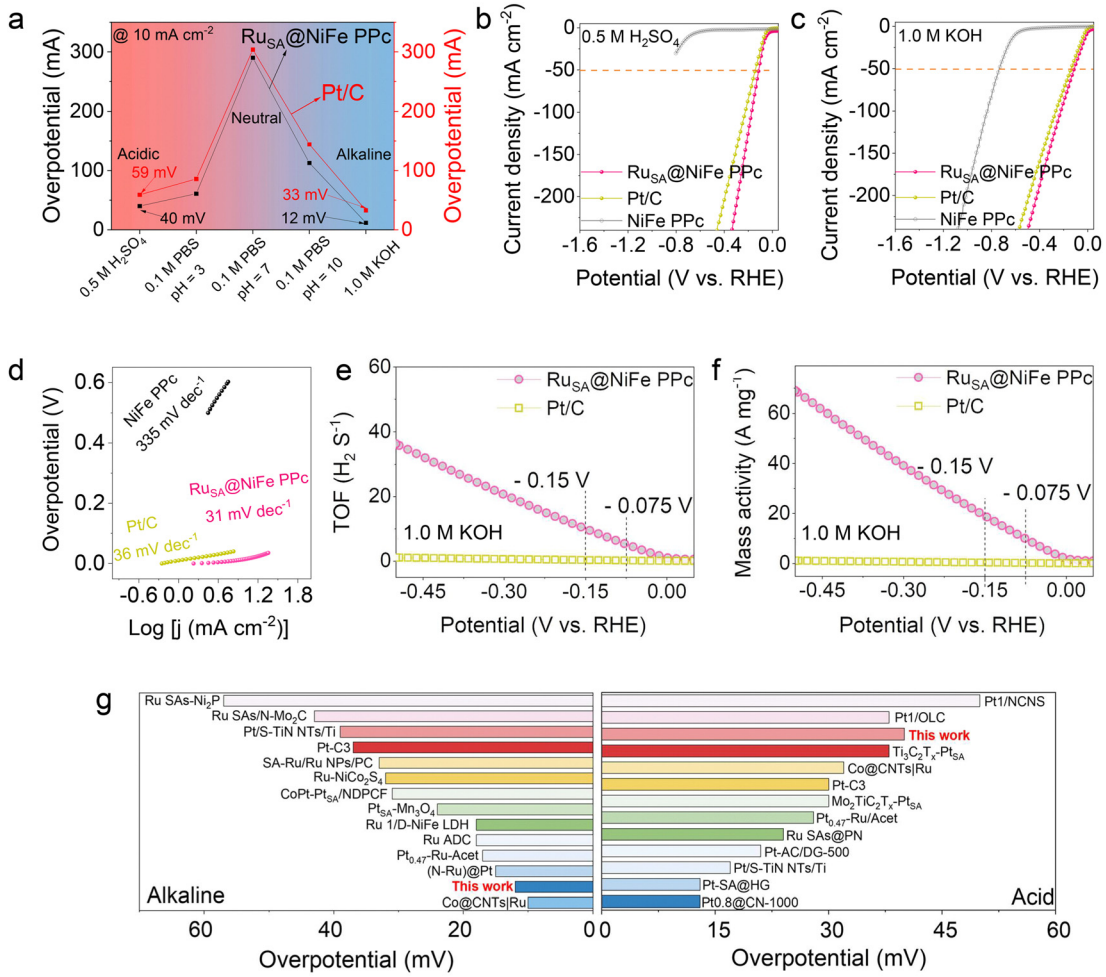

Fig. 3 Electrochemical hydrogen evolution performance. (a) The overpotential values of Ru_{SA}@NiFe PPc and Pt/C at 10 mA cm^{-2} in acid, neutral, and alkaline electrolytes. Polarization curves of Ru_{SA}@NiFe PPc, NiFe PPc, and Pt/C in (b) 0.5 M H_2SO_4 and (c) 1.0 M KOH. (d) Tafel slopes of Ru_{SA}@NiFe PPc, NiFe PPc, and Pt/C. Calculated TOF (e) and mass activity (f) values of Ru_{SA}@NiFe PPc and Pt/C. (g) Comparison of overpotentials of different catalysts at 10 mA cm^{-2}, and the related references are listed in the ESI.†

R_{ct} value of Ru_{SA}@NiFe PPc was obviously lower and decreased faster than that of bare NiFe PPc with changing potential (Fig. S18c, ESI†), which suggests that oxygen-containing intermediates were rapidly adsorbed at low driving potentials to produce key recants. Thus, Ru_{SA}@NiFe PPc showed a fast kinetics of the HER process. Furthermore, *in situ* Bode phase plots with low-frequency and high-frequency regions that represented the interfacial charge transfer and inner-layer electron transport of electrocatalysts were recorded (Fig. S19, ESI†). Compared with the NiFe PPc, the rapid decrease of the phase angle peak at a low-frequency on Ru_{SA}@NiFe PPc verified the facilitated charge transfer after incorporating Ru atoms, which ultimately stimulates the HER kinetics. Furthermore, as for a quantitative comparison of Ru_{SA}@NiFe PPc and commercial Pt/C, the mass activity and turnover frequency (TOF) values were calculated. The Ru_{SA}@NiFe PPc exhibited a higher HER activity, with a notable TOF of 12.50 s^{-1} and mass activity of 23.10 A mg^{-1} in 0.5 M H_2SO_4, nearly 48 times and 92 times higher than 0.26 s^{-1} and 0.25 A mg^{-1} of commercial Pt/C, respectively (Fig. S20, ESI†). Under the alkaline conditions, the above test contents showed a similar trend (Fig. 3e and f). Additionally, the comparison of Ru_{SA}@NiFe PPc and other reported noble-metal-based catalysts further revealed the outstanding HER reactivity of Ru_{SA}@NiFe PPc (Fig. 3g and Table S1, ESI†).

A long-term stability test of Ru_{SA}@NiFe PPc was performed, and the results showed almost no decay at high current densities in a harsh environment (*e.g.*, 200 mA cm^{-2} in 0.5 M H_2SO_4 and 100 mA cm^{-2} in 1.0 M KOH for ~44 h) (Fig. 4a and b). And the high stability was also supported by the potential cycling test, in which only a negligible decay in HER performance after 2000 cycles was observed (Fig. 4c). We also recorded *in situ* Raman spectra to explore the structure evolution of the Ru_{SA}@NiFe PPc. As shown in Fig. S21 (ESI†), when the voltage range increased from +0.1 to −0.6 V, the *in situ* Raman-signals retained the primary modes without the appearance of new peaks, which confirmed the excellent structural stability of Ru_{SA}@NiFe PPc during the HER test. Besides, the post-reaction XRD results further illustrated that the Ru particles were absent in the Ru_{SA}@NiFe PPc (Fig. S6, ESI†). To further confirm the excellent structural stability, we conducted the ICP-OES tests to obtain the

content of metal ions in the electrolyte (Table S5, ESI†). The contents of metal elements (Ni, Fe, and Ru) in the electrolyte before and after the HER had a negligible change, which proved that the metals in the phthalocyanine network can be maintained under this condition.

To clarify the potential of Ru_{SA}@NiFe PPc for practical application, a two-electrode electrolyzer was constructed using Ru_{SA}@NiFe PPc and RuO_2 (Fig. S22a and b, ESI†), and the commercial Pt/C and RuO_2 as references. The cell voltage for Ru_{SA}@NiFe PPc (−)‖RuO_2 (+) to reach a current density of 10 mA cm^{-2} was lower than that of the benchmark electrolyzer cell of about 101 mV and 82 mV in 1.0 M KOH and 0.5 M H_2SO_4 (Fig. S23, ESI†), respectively. Meanwhile, the Ru_{SA}@NiFe PPc (−)‖RuO_2 (+) system exhibited a long-term electrochemical stability for about 11 h at 100 mA cm^{-2} (Fig. S22c, ESI†). Furthermore, proton exchange membrane water electrolysis (PEMWE) was performed by combining commercial IrO_2 as the anode with the Ru_{SA}@NiFe PPc cathode (Ru_{SA}@NiFe PPc‖IrO_2), the Pt/C‖IrO_2 and NiFe PPc‖IrO_2 acting as comparative systems (Fig. 5a). The Ru_{SA}@NiFe PPc‖IrO_2 system had a distinguished water splitting performance, achieving a 2.27 V cell voltage at 2.0 A cm^{-2}, which surpassed that of commercial system Pt/C‖IrO_2 with a low current density of 0.78 A cm^{-2} (Fig. 5b); meanwhile, the current density of the NiFe PPc‖IrO_2 system was 5.8 times lower than that of Ru_{SA}@NiFe PPc‖IrO_2 at a cell voltage of 2.27 V (Fig. 5c). Along this line, alkaline electrolysis was further conducted by using stainless steel mesh (SSM) as the anode with Ru_{SA}@NiFe PPc as the cathode (Ru_{SA}@NiFe PPc‖SSM). A coupled Ru_{SA}@NiFe PPc‖SSM system achieved current densities of 1.0 A cm^{-2} and 2.0 A cm^{-2} at cell voltages of 1.64 V and 1.72 V, respectively (Fig. S24, ESI†). In contrast, other coupled systems like commercial Pt/C‖SSM and commercial RANEY® nickel‖SSM were also analysed to compare their performances with that of Ru_{SA}@NiFe PPc‖SSM. Under the same test conditions, the cell voltage of commercial RANEY® nickel‖SSM and commercial Pt/C‖SSM systems exceeded that of Ru_{SA}@NiFe PPc‖SSM by about 270 mV and 70 mV, respectively, at the same current density of 1.0 A cm^{-2}. These above results suggested that Ru_{SA}@NiFe PPc can be used as a cathode candidate for effectively producing clean energy.

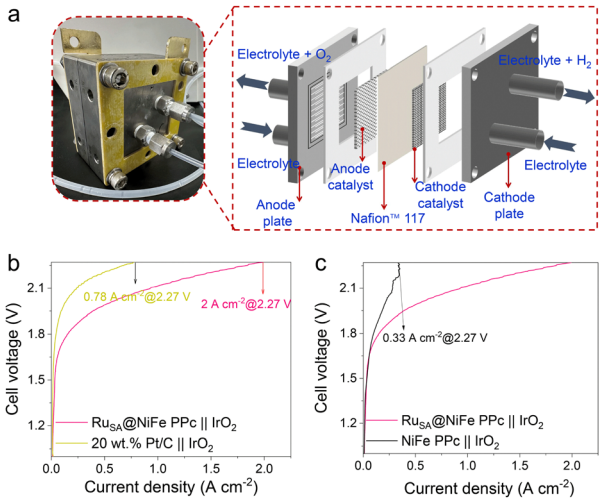

Fig. 5 Characterization of the water splitting device at the cell level. (a) The diagram of PEMWE assembly configuration. (b) and (c) Polarization curves of Ru_{SA}@NiFe PPc‖IrO_2, Pt/C‖IrO_2, and NiFe PPc‖IrO_2 systems in PEMWE.

To gain an in-depth insight into the HER activity contribution from immobilization of Ru atoms at Ru_{SA}@NiFe PPc, DFT calculations are performed. The structures of Ni PPc and Fe PPc are utilized as the calculation models (Fig. 6a). Firstly, the diagrams of charge density difference are used to clarify the tuning mechanism from the electronic state (Fig. 6a). The stronger electron aggregation phenomenon is found at the region of the Ru–N bonds, which clearly illustrate an efficient charge transfer between NiFe PPc and Ru atoms,[27] consistent with the experimental results. It further confirms that the electronic structure of NiFe PPc is modulated after introducing Ru atoms. According to the d-band center highly correlated with the metal adsorbate interaction, the density of states (DOS) is also calculated. In detail, the position of Ru 3d states in Ru@Fe PPc (−1.37 eV) relative to the Fermi level is lower than that of Ru@Ni PPc (−0.98 eV) (Fig. 6b), which indicates the stronger capability of capturing electrons for benefiting the reduction of H^+ and *H adsorption.[45] Besides, the local states near the Fermi levels of Ru@Ni PPc are significantly higher than that of the pristine catalyst, indicating that the anchored Ru atoms will lead to electron coupling and charge redistribution for optimizing the adsorption free energy of H* (ΔG_{H^*}).[46] Moreover, as illustrated in Fig. 6b, the Ru_{SA}@NiFe PPc shows higher occupied states than the NiFe PPc near the Fermi level, which is associated with promoted electron transfer leading to a higher conductivity. The comparison reveals that the

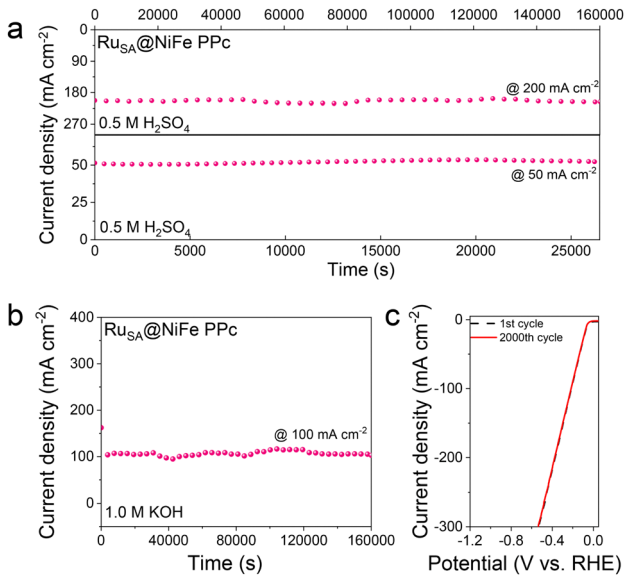

Fig. 4 Electrocatalyst stability evaluation. (a) Amperometric *i*–*t* measurements of Ru_{SA}@NiFe PPc at 50 and 200 mA cm^{-2} in 0.5 M H_2SO_4. (b) Amperometric *i*–*t* measurement of Ru_{SA}@NiFe PPc at 100 mA cm^{-2} in 1.0 M KOH. (c) Polarization curves of Ru_{SA}@NiFe PPc before and after 2000 cyclic voltammetry tests.

enhanced DOS near the Fermi level is mainly contributed by the Ru d orbitals (Fig. 6b), which indicates that the Ru single-atom can effectively improve the d-electron domination near the Fermi level, leading to enhanced HER activity.[30]

To further investigate the inherent relationship between the electronic structure and HER activity improvement of Ru_{SA}@NiFe PPc, the Gibbs free energy for elementary reaction steps in the HER is explored (Fig. 6c and d). Considering the Volmer–Tafel mechanism of the adsorption of two hydrogen ions,[47] the Ru@Ni PPc and Ru@Fe PPc exhibit minimum energy barriers in acidic media (Fig. 6c). Specifically, as compared with Ni PPc (1.90 eV) and Fe PPc (0.36 eV), the ΔG_{H^*} at the Ru sites on Ru@Ni PPc and Ru@Fe PPc possesses lower values of −0.49 eV and −0.30 eV, respectively, which indicates that the introduced Ru atoms have more favorable enthalpy of H* adsorption and simultaneous decrease in the thermodynamic barriers for the whole HER steps. Meanwhile, the free energy barrier of the rate-determining step of Ru@Ni PPc (−0.76 eV) and Ru@Fe PPc (−0.87 eV) dramatically decreases, as compared with Ni PPc (2.66 eV) and Fe PPc (1.40 eV) (Fig. 6c), indicating a more favorable HER kinetics for Ru_{SA}@NiFe PPc.

Unlike a only descriptor of ΔG_{H^*} under acidic conditions, the alkaline HER involving the adsorption and dissociation of water molecules and the supply of proton sources is more

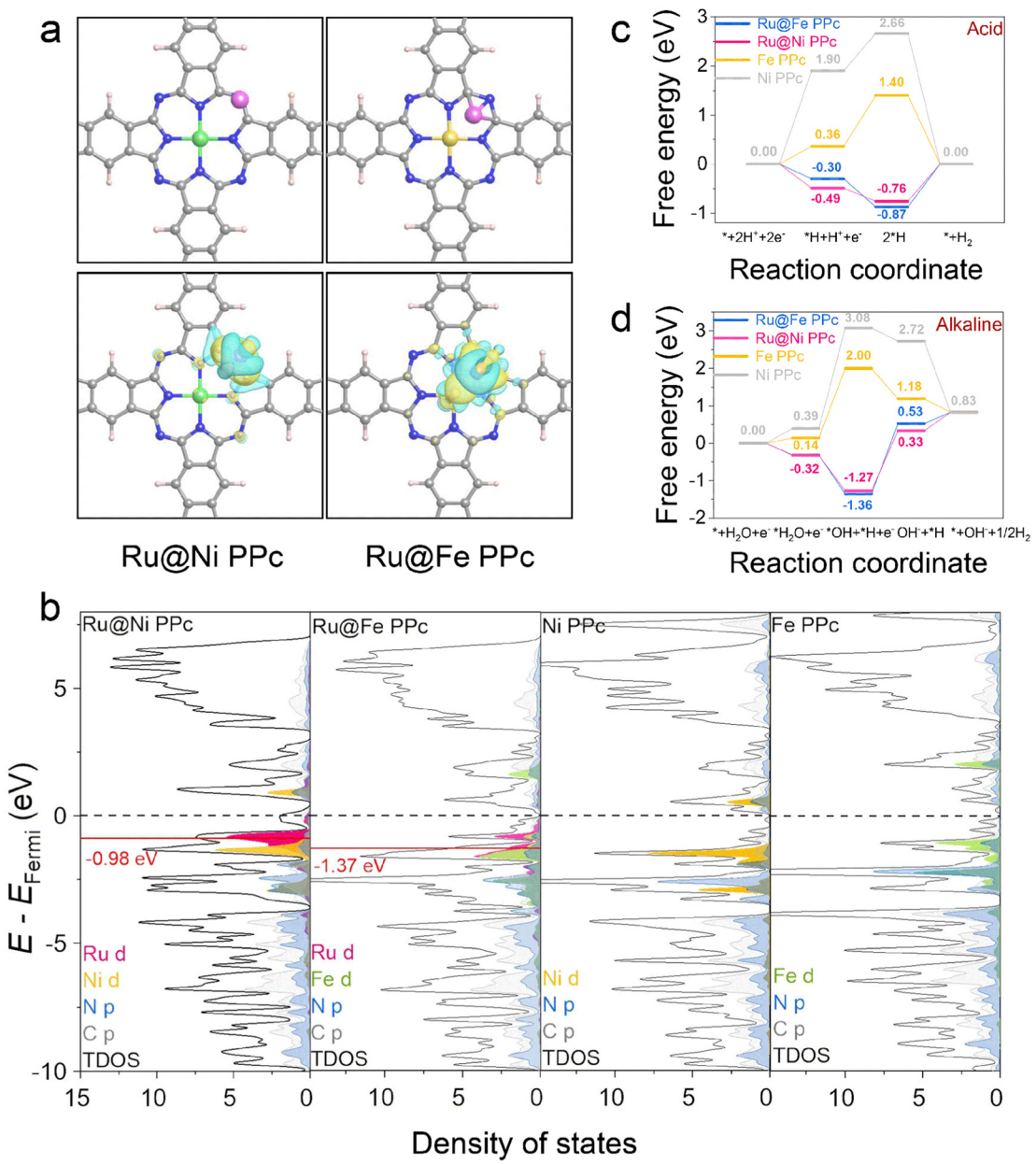

Fig. 6 Theoretical calculations. (a) Optimized structures of Ru@Ni PPc and Ru@Fe PPc and the charge density difference diagrams of Ru@Ni PPc and Ru@Fe PPc. (b) Calculated DOS of Ru@Ni PPc, Ru@Fe PPc, Ni PPc and Fe PPc; red lines illustrate the Ru d-band centers. (c) and (d) Calculated free energy diagrams of the HER process in acid and alkaline media for different samples.

complex. Therefore, we also calculate the other key activity parameters. Ru@Ni PPc and Ru@Fe PPc models show more negative adsorption energies of H_2O (~ -0.32 eV) compared with Ni PPc (0.39 eV) and Fe PPc (0.14 eV) (Fig. 6d), which suggests that the Ru atoms are beneficial to the adsorption and activation of H_2O. Subsequently, the H_2O^* undergoes the dissociation process, during which the energy barrier obviously decreases from 2.69 eV for Ni PPc and 1.86 eV for Fe PPc to 0.95 eV for Ru@Ni PPc and 1.04 eV for Ru@Fe PPc, thus the depressed Volmer step can be facilitated for generating the sufficient proton source. According to the above analysis, benefiting from the contribution of the d orbital of Ru and strong electronic coupling with the conjugate networks of NiFe PPc, the occupied states near the Fermi level and the electronic structure of the catalyst have been modulated. And the blocked activation/dissociation of H_2O and the adsorption/reduction of the *H process are jointly optimized, thus breaking the gap of HER kinetics under different conditions.

Conclusions

In summary, we have produced an all-pH HER electrocatalyst with enhanced activity by introducing Ru atoms into 2D NiFe PPc. Impressively, the as-prepared Ru_{SA}@NiFe PPc exhibited a superior all-pH HER performance and fast kinetics, achieving a small overpotential of 12 mV at 10 mA cm^{-2} and a low Tafel slope of 31 mV dec^{-1}, respectively, superior to that of commercial Pt/C. Through further exploration, we found the successful construction of Ru–N bridges between the Ru atoms and MPc interface, in which the strong electronic coupling between them effectively perturbed the electronic structure of metal phthalocyanine, proved by spectral characterization. DFT calculations revealed that the introduction of Ru atoms produced the favorable thermoneutral ΔG_{H^*} process and boosted the adsorption/activation of water through regulating the electronic structure of NiFe PPc, thus stimulating fast HER kinetics regardless of the reaction environments. This work opens up new opportunities for designing efficient CMP catalysts *via* bridging noble-metal atoms to modulate electronic structure and intermediate adsorption/desorption.

Conflicts of interest

There are no conflicts to declare.

Acknowledgements

Y. Hou acknowledges the financial support from the development project of Zhejiang Province's ''Jianbing'' and ''Lingyan'' (2023C01226), the National Natural Science Foundation of China (22278364, U22A20432, 22211530045, and 22178308), the National Key Research and Development Program of China (2022YFB4002100), the Fundamental Research Funds for the Central Universities (226-2022-00044, 226-2022-00055), the Science Foundation of Donghai Laboratory (DH-2022ZY0009), and the Startup Foundation for Hundred-Talent Program of Zhejiang University. T. Zhang acknowledges the Science Foundation of Donghai Laboratory (DH-2022KF0310), the Excellent Youth Foundation of Zhejiang Province of China (LR21E030001), the Leading Innovative and Entrepreneur Team Introduction Program of Zhejiang (2021R01005), the National Natural Science Foundation of China (52003279), and the Key Research and Development Program of Ningbo (2022ZDYF020023).

Notes and references

1 J. Chen, *et al.*, Reversible hydrogen spillover in Ru–WO_{3-x} enhances hydrogen evolution activity in neutral pH water splitting, *Nat. Commun.*, 2022, **13**, 5382.
2 M. Qin, *et al.*, Elucidating electrocatalytic mechanism for large-scale cycloalkanol oxidation integrated with hydrogen evolution, *Chem. Eng. J.*, 2022, **442**, 136264–136274.
3 Z. Seh, *et al.*, Combining theory and experiment in electrocatalysis: insights into materials design, *Science*, 2017, **355**, eaad4998.
4 A. H. Shah, *et al.*, The role of alkali metal cations and platinum-surface hydroxyl in the alkaline hydrogen evolution reaction, *Nat. Catal.*, 2022, **5**, 923–933.
5 Y. Zhao, *et al.*, Modulating Pt–O–Pt atomic clusters with isolated cobalt atoms for enhanced hydrogen evolution catalysis, *Nat. Commun.*, 2022, **13**, 2430.
6 X. Zou, *et al.*, Noble metal-free hydrogen evolution catalysts for water splitting, *Chem. Soc. Rev.*, 2015, **44**, 5148–5180.
7 J. Mahmood, *et al.*, An efficient and pH-universal ruthenium-based catalyst for the hydrogen evolution reaction, *Nat. Nanotechnol.*, 2017, **12**, 441–446.
8 Y. Zhao, *et al.*, Constructing atomic heterometallic sites in ultrathin nickel-incorporated cobalt phosphide nanosheets via a boron-assisted strategy for highly efficient water splitting, *Nano Lett.*, 2021, **21**, 823–832.
9 J. Luo, *et al.*, Water photolysis at 12.3% efficiency via perovskite photovoltaics and earth-abundant catalysts, *Science*, 2014, **345**, 1593.
10 P. Nikolaidis, *et al.*, A comparative overview of hydrogen production processes, *Renewable Sustainable Energy Rev.*, 2017, **67**, 597–611.
11 T. Wang, *et al.*, Combined anodic and cathodic hydrogen production from aldehyde oxidation and hydrogen evolution reaction, *Nat. Catal.*, 2022, **5**, 66–73.
12 S. Z. Oener, *et al.*, Accelerating water dissociation in bipolar membranes and for electrocatalysis, *Science*, 2020, **369**, 1099–1103.
13 C. Pei, *et al.*, Electron transfer-induced metal spin-crossover at $NiCo_2S_4/ReS_2$ 2D-2D interfaces for promoting pH-universal hydrogen evolution reaction, *Adv. Funct. Mater.*, 2023, **33**, 2210072.
14 C. Tang, *et al.*, NiSe nanowire film supported on nickel foam: an efficient and stable 3D bifunctional electrode for full water splitting, *Angew. Chem., Int. Ed.*, 2015, **54**, 9351.
15 H. Wang, *et al.*, Bifunctional non-noble metal oxide nanoparticle electrocatalysts through lithium-induced conversion for overall water splitting, *Nat. Commun.*, 2015, **6**, 7261.

16 T. Zhang, *et al.*, Pinpointing the axial ligand effect on platinum single-atom-catalyst towards efficient alkaline hydrogen evolution reaction, *Nat. Commun.*, 2022, **13**, 6875.
17 I. L. Yanez, *et al.*, Interfacial water reorganization as a pH-dependent descriptor of the hydrogen evolution rate on platinum electrodes, *Nat. Energy*, 2017, **2**, 17031.
18 V. R. Stamenkovic, *et al.*, Energy and fuels from electrochemical interfaces, *Nat. Mater.*, 2017, **16**, 57–69.
19 L. Zhang, *et al.*, Atomic layer deposited Pt–Ru dual-metal dimers and identifying their active sites for hydrogen evolution reaction, *Nat. Commun.*, 2019, **10**, 4936.
20 N. Cheng, *et al.*, Platinum single-atom and cluster catalysis of the hydrogen evolution reaction, *Nat. Commun.*, 2016, **7**, 13638.
21 K. Chen, *et al.*, Iron phthalocyanine with coordination induced electronic localization to boost oxygen reduction reaction, *Nat. Commun.*, 2020, **11**, 4173.
22 R. Wang, *et al.*, Proton/electron donors enhancing electrocatalytic activity of supported conjugated microporous polymers for CO_2 reduction, *Angew. Chem., Int. Ed.*, 2021, **61**, e202115503.
23 J. S. Lee, *et al.*, Advances in conjugated microporous polymers, *Chem. Rev.*, 2020, **120**, 2171–2214.
24 S. Yang, *et al.*, Recent advances in electrocatalysis with phthalocyanines, *Chem. Soc. Rev.*, 2021, **50**, 12985–13011.
25 M. Wang, *et al.*, An efficient interfacial synthesis of two-dimensional metal-organic framework nanosheets for electrochemical hydrogen peroxide production, *Angew. Chem., Int. Ed.*, 2021, **60**, 11190–11195.
26 W. Li, *et al.*, Advanced bifunctional oxygen reduction and evolution electrocatalyst derived from surface-mounted metal-organic frameworks, *Angew. Chem., Int. Ed.*, 2020, **59**, 5837–5843.
27 Y. Sun, *et al.*, Modulating electronic structure of metal-organic frameworks by introducing atomically dispersed Ru for efficient hydrogen evolution, *Nat. Commun.*, 2021, **12**, 1369.
28 Z. Lei, *et al.*, Coordination modulation of iridium single-atom catalyst maximizing water oxidation activity, *Nat. Commun.*, 2022, **13**, 24.
29 P. Zhai, *et al.*, Engineering single-atomic ruthenium catalytic sites on defective nickel-iron layered double hydroxide for overall water splitting, *Nat. Commun.*, 2021, **12**, 4587.
30 J. Zhang, *et al.*, Single platinum atoms immobilized on an MXene as an efficient catalyst for the hydrogen evolution reaction, *Nat. Catal.*, 2018, **1**, 985–992.
31 Q. Hu, *et al.*, Subnanometric Ru clusters with upshifted d band center improve performance for alkaline hydrogen evolution reaction, *Nat. Commun.*, 2022, **13**, 3958.
32 K. Wang, *et al.*, Highly active ruthenium sites stabilized by modulating electron-feeding for sustainable acidic oxygen-evolution electrocatalysis, *Energy Environ. Sci.*, 2022, **15**, 2356–2365.
33 L. Wang, *et al.*, Electronic modulation of metal-organic frameworks by interfacial bridging for efficient pH-universal hydrogen evolution, *Adv. Funct. Mater.*, 2023, **33**, 221032.
34 H. Sun, *et al.*, Topotactically transformed polygonal mesopores on ternary layered double hydroxides exposing under-coordinated metal centers for accelerated water dissociation, *Adv. Mater.*, 2020, **32**, 2006784.
35 Z. Kou, *et al.*, Bridging heterogeneous and homogeneous catalysts by ultrathin metal-polyphthalocyanine-based nanosheets from electron-coupled transalkylation delamination, *Nano Energy*, 2022, **98**, 107297.
36 S. Yang, *et al.*, Two-dimensional conjugated aromatic networks as high-site-density and single-atom electrocatalysts for the oxygen reduction reaction, *Angew. Chem., Int. Ed.*, 2019, **58**, 14724–14730.
37 Q. Qi, *et al.*, Large-scale synthesis of low-cost bimetallic polyphthalocyanine for highly stable water oxidation, *Appl. Catal., B*, 2021, **299**, 120637.
38 K. Jiang, *et al.*, Single platinum atoms embedded in nanoporous cobalt selenide as electrocatalyst for accelerating hydrogen evolution reaction, *Nat. Commun.*, 2019, **10**, 1743.
39 J. Yan, *et al.*, Single atom tungsten doped ultrathin α-$Ni(OH)_2$ for enhanced electrocatalytic water oxidation, *Nat. Commun.*, 2019, **10**, 2149.
40 V. Ramalingam, *et al.*, Heteroatom-mediated interactions between ruthenium single atoms and an MXene support for efficient hydrogen evolution, *Adv. Mater.*, 2019, **31**, 1903841.
41 K. Kamiya, *et al.*, Platinum-modified covalent triazine frameworks hybridized with carbon nanoparticles as methanol-tolerant oxygen reduction electrocatalysts, *Nat. Commun.*, 2014, **5**, 5040.
42 K. Wu, *et al.*, Atomically dispersed Ni–Ru–P interface sites for high-efficiency pH-universal electrocatalysis of hydrogen evolution, *Nano Energy*, 2021, **80**, 105467.
43 H. Su, *et al.*, In situ electronic redistribution tuning of $NiCo_2S_4$ nanosheets for enhanced electrocatalysis, *Adv. Funct. Mater.*, 2022, **32**, 2109731.
44 J. Chen, *et al.*, Inner Co synergizing outer Ru supported on carbon nanotubes for efficient pH-universal hydrogen evolution catalysis, *Nano-Micro Lett.*, 2022, **14**, 186.
45 Z. Wei, *et al.*, Reversed charge transfer and enhanced hydrogen spillover in platinum nanoclusters anchored on titanium oxide with rich oxygen vacancies boost hydrogen evolution reaction, *Angew. Chem., Int. Ed.*, 2021, **60**, 16622–16627.
46 X. Zhang, *et al.*, Molybdenum phosphide/carbon nanotube hybrids as pH-universal electrocatalysts for hydrogen evolution reaction, *Adv. Funct. Mater.*, 2018, **28**, 1706523.
47 J. D. Benck, *et al.*, Catalyzing the hydrogen evolution reaction (HER) with molybdenum sulfide nanomaterials, *ACS Catal.*, 2014, **4**, 3957–3971.